



DESI $z \gtrsim 5$ Quasar Survey. I. A First Sample of 400 New Quasars at $z \sim 4.7\text{--}6.6$

Jinyi Yang^{1,34} , Xiaohui Fan¹ , Ansh Gupta¹ , Adam D. Myers², Nathalie Palanque-Delabrouille^{3,4} , Feige Wang^{1,35} ,
 Christophe Yèche⁴, Jessica Nicole Aguilar³, Steven Ahlen⁵ , David M. Alexander⁶, David Brooks⁷, Kyle Dawson⁸ ,
 Axel de la Macorra⁹, Arjun Dey¹⁰ , Govinda Dhungana¹¹ , Kevin Fanning^{12,13,14}, Andreu Font-Ribera¹⁵ , Satya Gontcho³ ,
 Julien Guy³, Klaus Honscheid^{13,16,17}, Stephanie Juneau¹⁰ , Theodore Kisner³ , Anthony Kremin³ , Laurent Le Guillou¹⁸ ,
 Michael Levi³ , Christophe Magneville⁴, Paul Martini^{13,16,19} , Aaron Meisner²⁰ , Ramon Miquel^{15,21} , John Moustakas²² ,
 Jundan Nie²³ , Will Percival^{24,25,26} , Claire Poppett^{3,27,28}, Francisco Prada²⁹ , Edward Schlafly³⁰ , Gregory Tarlé¹⁴ ,
 Mariana Vargas Magana⁹, Benjamin Alan Weaver²⁰, Risa Wechsler^{31,32,33} , Rongpu Zhou³ , Zhimin Zhou²³ , and Hu Zou²³

¹Steward Observatory, University of Arizona, 933 North Cherry Avenue, Tucson, AZ 85721, USA; jinyiyang@email.arizona.edu

²Department of Physics & Astronomy, University of Wyoming, 1000 East University, Dept. 3905, Laramie, WY 82071, USA

³Lawrence Berkeley National Laboratory, 1 Cyclotron Road, Berkeley, CA 94720, USA

⁴IRFU, CEA, Université Paris-Saclay, F-91191 Gif-sur-Yvette, France

⁵Physics Dept., Boston University, 590 Commonwealth Avenue, Boston, MA 02215, USA

⁶Centre for Extragalactic Astronomy, Department of Physics, Durham University, South Road, Durham, DH1 3LE, UK

⁷Department of Physics & Astronomy, University College London, Gower Street, London, WC1E 6BT, UK

⁸Department of Physics and Astronomy, The University of Utah, 115 South 1400 East, Salt Lake City, UT 84112, USA

⁹Instituto de Física, Universidad Nacional Autónoma de México, Cd. de México C.P. 04510, Mexico

¹⁰National Science Foundation's National Optical-Infrared Astronomy Research Laboratory, 950 North Cherry Avenue, Tucson, AZ 85719, USA

¹¹Department of Physics, Southern Methodist University, 3215 Daniel Avenue, Dallas, TX 75275, USA

¹²Department of Physics, University of Michigan, Ann Arbor, MI 48109, USA

¹³The Ohio State University, Columbus, 43210 OH, USA

¹⁴University of Michigan, Ann Arbor, MI 48109, USA

¹⁵Institut de Física d'Altes Energies (IFAE), The Barcelona Institute of Science and Technology, Campus UAB, E-08193 Bellaterra, Barcelona, Spain

¹⁶Center for Cosmology and AstroParticle Physics, The Ohio State University, 191 West Woodruff Avenue, Columbus, OH 43210, USA

¹⁷Department of Physics, The Ohio State University, 191 West Woodruff Avenue, Columbus, OH 43210, USA

¹⁸Sorbonne Université, CNRS/IN2P3, Laboratoire de Physique Nucléaire et de Hautes Energies (LPNHE), F-75005 Paris, France

¹⁹Department of Astronomy, The Ohio State University, 4055 McPherson Laboratory, 140 West 18th Avenue, Columbus, OH 43210, USA

²⁰NSF's NOIRLab, 950 North Cherry Avenue, Tucson, AZ 85719, USA

²¹Institució Catalana de Recerca i Estudis Avançats, Passeig de Lluís Companys, 23, E-08010 Barcelona, Spain

²²Department of Physics and Astronomy, Siena College, 515 Loudon Road, Loudonville, NY 12211, USA

²³National Astronomical Observatories, Chinese Academy of Sciences, A20 Datun Road, Chaoyang District, Beijing, 100012, People's Republic of China

²⁴Department of Physics and Astronomy, University of Waterloo, 200 University Ave West, Waterloo, ON N2L 3G1, Canada

²⁵Perimeter Institute for Theoretical Physics, 31 Caroline Street North, Waterloo, ON N2L 2Y5, Canada

²⁶Waterloo Centre for Astrophysics, University of Waterloo, 200 University Avenue W, Waterloo, ON N2L 3G1, Canada

²⁷Space Sciences Laboratory, University of California, Berkeley, 7 Gauss Way, Berkeley, CA 94720, USA

²⁸University of California, Berkeley, 110 Sproul Hall #5800, Berkeley, CA 94720, USA

²⁹Instituto de Astrofísica de Andalucía (CSIC), Glorieta de la Astronomía, s/n, E-18008 Granada, Spain

³⁰Space Telescope Science Institute, 3700 San Martin Drive, Baltimore, MD 21218, USA

³¹Kavli Institute for Particle Astrophysics and Cosmology, Stanford University, Menlo Park, CA 94305, USA

³²Physics Department, Stanford University, Stanford, CA 93405, USA

³³SLAC National Accelerator Laboratory, Menlo Park, CA 94305, USA

Received 2023 February 2; revised 2023 August 17; accepted 2023 August 31; published 2023 November 6

Abstract

We report the first results of a high-redshift ($z \gtrsim 5$) quasar survey using the Dark Energy Spectroscopic Instrument (DESI). As a DESI secondary target program, this survey is designed to carry out a systematic search and investigation of quasars at $4.8 < z < 6.8$. The target selection is based on the DESI Legacy Imaging Surveys (the Legacy Surveys) DR9 photometry, combined with the Pan-STARRS1 data and J -band photometry from public surveys. A first quasar sample has been constructed from the DESI Survey Validation 3 (SV3) and first-year observations until 2022 May. This sample includes more than 400 new quasars at redshift $4.7 \leq z < 6.6$, down to 21.5 magnitude (AB) in the z band, discovered from 35% of the entire target sample. Remarkably, there are 220 new quasars identified at $z \geq 5$, more than one-third of existing quasars previously published at this redshift. The observations so far result in an average success rate of 23% at $z > 4.7$. The current spectral data set has already allowed analysis of interesting individual objects (e.g., quasars with damped Ly α absorbers and broad absorption line features), and statistical analysis will follow the survey's completion. A set of science projects will be carried out leveraging this program, including quasar luminosity function, quasar clustering, intergalactic medium, quasar spectral properties, intervening absorbers, and properties of early supermassive black holes. Additionally, a sample

³⁴ Strittmatter Fellow.

³⁵ NASA Hubble Fellow.



Original content from this work may be used under the terms of the [Creative Commons Attribution 4.0 licence](https://creativecommons.org/licenses/by/4.0/). Any further distribution of this work must maintain attribution to the author(s) and the title of the work, journal citation and DOI.

of 38 new quasars at $z \sim 3.8\text{--}5.7$ discovered from a pilot survey in the DESI SV1 is also published in this paper.

Unified Astronomy Thesaurus concepts: [Quasars \(1319\)](#); [Surveys \(1671\)](#); [Broad absorption line quasar \(183\)](#)

Supporting material: figure set, machine-readable tables

1. Introduction

Quasars at $z \gtrsim 5$, residing in the cosmic times from the reionization era to the post-reionization epoch, are unique probes of the intergalactic medium (IGM) evolution during the last stage of the neutral hydrogen phase transition in the IGM (e.g., Eilers et al. 2018; Yang et al. 2020b; Bosman et al. 2022) and the growth of early supermassive black holes (SMBH; e.g., Shen et al. 2019; Yang et al. 2021; Farina et al. 2022). The study of quasar luminosity function and black hole mass function over cosmic epochs tracks SMBH accretions (e.g., Shen & Kelly 2012; Kelly & Shen 2013). In addition, luminous high-redshift quasars are thought to trace the most massive dark matter halos in the young Universe (e.g., Costa et al. 2014). These luminous background sources also provide valuable sightlines for the investigations of intervening high-redshift H I in the circumgalactic medium or interstellar medium, e.g., the damped Ly α (DLA) absorbers, and metal absorbers (e.g., Chen et al. 2017; D’Odorico et al. 2018).

Recent successful high-redshift quasar surveys have increased the number of known $z \geq 5$ quasars to ~ 600 (e.g., Fan et al. 2006; Willott et al. 2010; Mortlock et al. 2011; Venemans et al. 2015; Wu et al. 2015; Bañados et al. 2016; Jiang et al. 2016; Mazzucchelli et al. 2017; McGreer et al. 2018; Reed et al. 2019; Matsuoka et al. 2019a, 2019b; Wang et al. 2016, 2018, 2019; Yang et al. 2017, 2019a, 2019b; Ross & Cross 2020; Yang et al. 2021), with the three most distant quasars at $z > 7.5$ (Bañados et al. 2018; Yang et al. 2020a; Wang et al. 2021). After the end of high-redshift quasar searches using the Sloan Digital Sky Survey I–IV (e.g., Schneider et al. 2010; Pâris et al. 2017; Lyke et al. 2020), recent discoveries of high-redshift quasars are mainly based on single-object observations, which have a limited efficiency of spectroscopy. As a result, most existing high-redshift quasar surveys either focus on luminous quasars in a wide field (e.g., Bañados et al. 2016; Wang et al. 2016; Yang et al. 2017) or target faint objects in a smaller area (e.g., McGreer et al. 2018; Matsuoka et al. 2019a). The Dark Energy Spectroscopic Instrument (DESI; Abareshi et al. 2022) employs a set of 10 multifiber spectrographs with wide spectral coverage, offering a unique opportunity to search for high-redshift quasars with high spectroscopic efficiency. The combination of deep wide-field imaging from the DESI Legacy Imaging Surveys (Dey et al. 2019, hereafter the Legacy Surveys) and DESI multi-object spectroscopy will allow a new wide-field survey of high-redshift quasars, extending through the entire DESI footprint and to a fainter luminosity range.

In this paper, we report a DESI secondary program designed to search for quasars at $z \sim 4.8\text{--}6.8$ using DESI. This is our program’s first publication to introduce the survey and publish discoveries from the DESI observations by 2022 May. We will describe the photometric data sets and target selection in Section 2. We will then report the observations and the first sample of new quasars in Section 3. In Section 3, we will also present examples of scientific analyses using the current quasar spectra. In Section 4, in addition to a summary, we will discuss

the future science projects using quasars from this survey. Additionally, we also publish a sample of new quasars from a pilot program of searching for $z \sim 4\text{--}5.3$ quasars during the DESI Survey Validation (SV) observations, which will be briefly described in Section 2. In this paper, we adopt a Λ CDM cosmology with parameters $\Omega_\Lambda = 0.7$, $\Omega_m = 0.3$, and $H_0 = 70 \text{ km s}^{-1} \text{ Mpc}^{-1}$. Photometric data in the optical are reported in the AB system after applying the Galactic extinction correction (Schlegel et al. 1998; Schlafly & Finkbeiner 2011); photometric data from infrared surveys (e.g., in J , $W1$, and $W2$ bands) are on the Vega system.

2. A High-redshift Quasar Survey in DESI

The DESI survey is designed to determine the nature of dark energy through the most precise measurement of the expansion history of the Universe (Levi et al. 2013). With 5000 fibers mounted in the focal plate and a 3° diameter field of view (DESI Collaboration et al. 2016b; Silber et al. 2023), DESI will measure the spectra of about 40 million galaxies and quasars covering 14,000 square degrees over its 5 yr observing campaign (DESI Collaboration et al. 2016a; Abareshi et al. 2022). DESI target selection is based on the imaging data from the Legacy Surveys (Zou et al. 2017; Dey et al. 2019; D. Schlegel et al. 2023, in preparation), including targets of the Milky Way Survey (Allende Prieto et al. 2020; Cooper et al. 2023), the Bright Galaxy Survey (Ruiz-Macias et al. 2020; Hahn et al. 2023), the Luminous Red Galaxy sample (Zhou et al. 2020, 2023), the Emission Line Galaxy sample (Raichoor et al. 2020, 2023), and the quasar (QSO) sample (Yèche et al. 2020; Chaussidon et al. 2023). The details of the pipelines designed for DESI target selections, fiber assignments, survey operations, spectral reduction, and spectral classifications can be found in Myers et al. (2023), A. Raichoor et al. (2023, in preparation), Guy et al. (2023), Schlafly et al. (2023), and S. Bailey et al. (2023, in preparation). The DESI survey will not only use quasars as direct tracers of the matter distribution mostly at $z < 2.1$, but also use quasars at $z > 2.1$ as backlights for the intervening matter distribution via the Ly α forest. The quasar selection for the DESI main survey is based on a random forest algorithm and is mainly focused on quasars at $z \lesssim 4.5$ (Chaussidon et al. 2023).

We present an additional quasar survey program designed to systematically search for quasars at $z \gtrsim 5$ using DESI, which is part of the DESI secondary target program of the DESI survey. More details of DESI secondary target programs and the DESI target pipeline can be found in Myers et al. (2023). The wide spectral coverage (3600–9800 Å) and high efficiency of the DESI spectrographs allow sensitive identification of quasar Ly α lines up to redshift ~ 6.8 (covering wavelength range blueward of 1250 Å in the rest frame). In addition, DESI’s spectral resolution ($R \sim 3000\text{--}5000$ at $\lambda > 5500$ Å) is higher than that of typical discovery spectra ($R \lesssim 1000$) used in most other high-redshift quasar surveys. Thus, the DESI spectra can be used to directly construct a data set for a wide range of scientific analyses with no need of

optical follow-up spectroscopy. For example, a complete DESI spectral data set of $z \gtrsim 5$ quasars will allow us to investigate quasar luminosity function, quasar clustering, quasar rest-frame UV spectral properties, IGM evolution, and intervening absorbers, as well as early supermassive black hole growth, together with multiwavelength follow-up observations.

2.1. Photometric Data Sets

The candidate selection of our survey is mainly based on the photometric data from the Legacy Surveys (Dey et al. 2019; D. Schlegel et al. 2023, in preparation), which images more than 19,700 square degrees of the extragalactic sky visible from the Northern Hemisphere in the g , r , and z bands. The Legacy Surveys consists of three programs: the Beijing-Arizona Sky Survey (BASS; Zou et al. 2017), covering an area in the North Galactic Cap with decl. $> 32.375^\circ$ in g and r bands; the Mayall z -band Legacy Survey (MzLS; Dey et al. 2019), imaging the same area as BASS in z band; and the Dark Energy Camera Legacy Survey (DECaLS; Dey et al. 2019), mapping the entire South Galactic Cap and the regions in North Galactic Cap with decl. $< 34^\circ$ in g , r , and z bands. There are also other public DECam grz data within the DESI footprint, such as the data from the Dark Energy Survey (DES; The Dark Energy Survey Collaboration 2005), which overlaps with the Legacy Surveys in an area of 1130 deg^2 . The Legacy Surveys program makes use of the DES raw data instead of reobserving that area.

The Legacy Surveys DR9³⁶ includes images in all the three bands with ≥ 3 observational passes over 14,750 square degrees, with median point-spread function (PSF) depth of 24.7 (24.2 in BASS area), 24.2 (23.7 in BASS), and 23.3 in the g , r , and z bands, respectively. The optical data are complemented by photometry in infrared bands ($W1$ and $W2$) from the all-sky data of the Wide-field Infrared Survey Explorer (WISE; Wright et al. 2010). The $W1$ and $W2$ data in the Legacy Surveys catalog are based on forced photometry in the unWISE images at the locations of the Legacy Surveys optical sources. The unWISE images are the unblurred coadds of WISE (Meisner et al. 2017, 2018), including all imaging through year 6 of NEOWISE-Reactivation (Mainzer et al. 2014).

We have also included photometric data from the Pan-STARRS1 survey (PS1; Chambers et al. 2016), which covers the 3π sky at decl. $> -30^\circ$ in the optical $grizy$ bands. In our survey, the PS1 i -band photometry is required for target selection, and data in PS1 z and y bands are included if available (see details in the next section). The PS1 survey has 5σ depth of 23.1, 22.3, and 21.4 mag in the i , z , and y bands, respectively. In the following discussions of color selection, we use z to represent the z -band photometric data from the Legacy Surveys and use z_{P1} for the PS1 photometry.

In addition, to further reduce contamination rate of quasar selection, photometric data in the near-infrared (NIR) J band are used for objects with available J -band photometry. We collect J -band data from the three public large-area NIR imaging surveys: the UKIRT Hemisphere Survey (UHS; Dye et al. 2018), the UKIRT InfraRed Deep Sky Surveys–Large Area Survey (ULAS; Lawrence et al. 2007), and the VISTA Hemisphere Survey (VHS; McMahon et al. 2013). UHS and

ULAS cover an area of 17,900 square degrees in the northern sky with a depth of 19.6 mag (Vega) in J . The VHS aims to map the entire southern sky and has a depth of 20.2 mag (Vega) in the J band.

2.2. DESI Survey of Quasars at $z \sim 4.8\text{--}6.8$

The quasar selection of our survey is based on optical-infrared color cuts, which have been previously applied to successful $z \sim 5\text{--}6.5$ quasar surveys (e.g., Bañados et al. 2016; Wang et al. 2016; Yang et al. 2017, 2019a, 2019b; Wang et al. 2019). We start our selection with the Legacy Surveys DR9 catalog and first apply a set of standard cuts: (1) BRICK_PRIMARY = T to select objects within the brick boundary; (2) MASKBITS not in [1, 10, 12, 13], which requires that the targets do not touch pixels in the vicinity of bright stars, “bailout” blobs (areas leading to fitting issues due to a very high source density), large galaxies, or globular clusters; (3) TYPE = PSF OR (dchisq[1]—dchisq[0])/dchisq[0] < 0.01 to select objects with stellar morphology. We next require that all targets should be observed in all bands and limit the signal-to-noise ratio (S/N) in the z ($> 5\sigma$), $W1$ ($> 3\sigma$), and $W2$ ($> 2\sigma$) bands. Then we apply very relaxed cuts in the gr bands (i.e., $S/N_g < 5$ or $g > 24.5$ or $g - r > 1.8$; $S/N_r < 5$ or $r - z > 1.0$) to reduce the sample size. These generate a preselected sample with ~ 13 million sources within the DESI footprint for following color-color selection.

One basic technique used for the color selection of high-redshift quasars is based on color “dropout,” which is caused by the $\text{Ly}\alpha$ break in quasar spectra due to significant IGM absorption at the wavelength blueward of the $\text{Ly}\alpha$ emission line at these redshifts. The $\text{Ly}\alpha$ line of a $z \sim 5$ quasar is located in the i band (7294.02 Å at $z = 5$). Thus, the i band is typically used as a detection band for the selection of $z \sim 5$ quasars, and the g and r are the dropout bands. At $z \gtrsim 5.7$, $\text{Ly}\alpha$ line moves into the z band and the i band becomes the dropout band, so the i band also plays a critical role in the selection of $z \sim 6$ quasars. We therefore include the i -band photometric data from the PS1 survey.

We crossmatch the preselected sample selected above with the PS1 DR1 and DR2 catalogs. We only use DR1 data when an object is not in the DR2 catalog but is in the DR1. Then we build up different selection criteria for three redshift ranges, $z \sim 4.8\text{--}5.4$, $5.7\text{--}6.4$, and $6.4\text{--}6.8$, according to the quasar color tracks in different color-color spaces. The main color-color selections are the $r - i/i - z$ for $z \sim 5$ and 6, and the $z - y/y - W1$ for $z \sim 6$ and 6.5. The $z - W1/W1 - W2$ color cuts are used for all redshifts. The redshift range of $z \sim 5.4\text{--}5.6$ is the redshift at which quasar locations fully overlap with those of middle-type M dwarfs in the riz color-color space. Multiple NIR colors are necessary to select quasars in this redshift range, as demonstrated in our previous successful $z \sim 5.5$ quasar survey (Yang et al. 2017, 2019a). Thus we exclude this redshift range in this survey. Below we briefly describe our selections of quasars in the three redshift ranges, and show the main color-color diagrams in Figures 1 and 2. The selection criteria are listed in Appendix A.

$z \sim 4.8\text{--}5.4$ quasar candidates. (1) We first select objects with g -band dropout by applying the cuts of $S/N_g < 3$ or $g - r > 2.5$. (2) We next require objects to have $> 5\sigma$ detection in the i_{P1} band and apply the $r - i/i - z$ color cuts as shown in Figure 1. (3) Then we apply the

³⁶ <https://www.legacysurvey.org/dr9/>

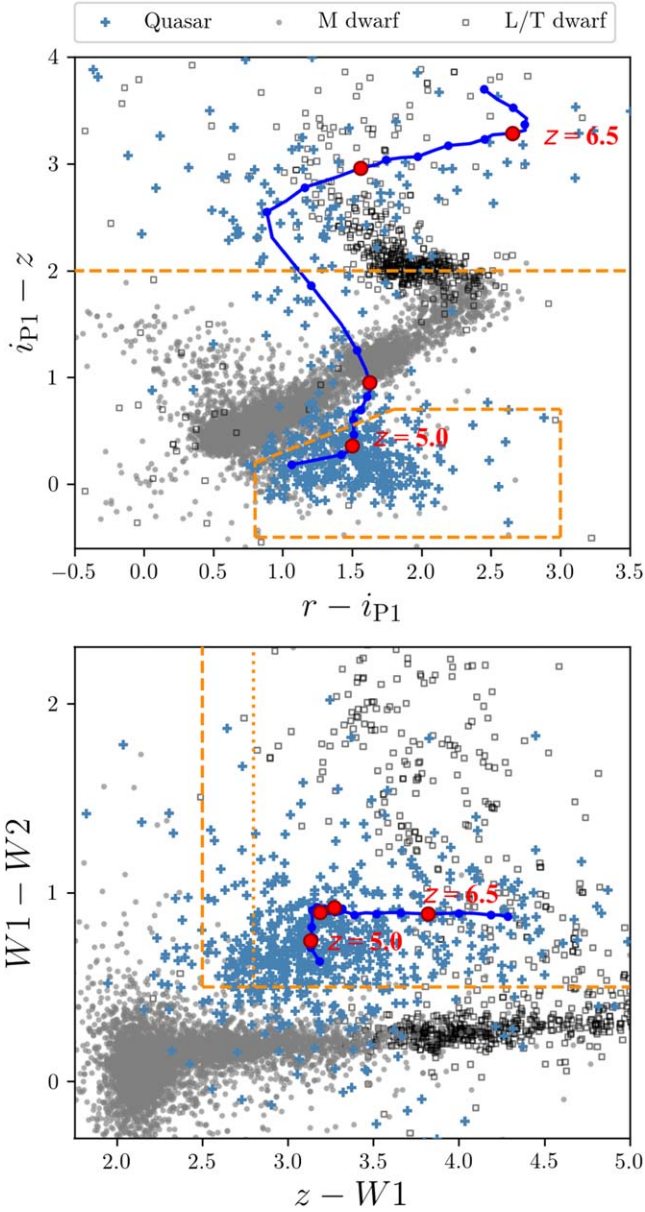


Figure 1. Top: the riz color-color diagram used for the quasar selection. The blue solid line shows the color track of quasars from $z = 4.8$ to $z = 6.8$ with a step of 0.1 (blue filled circles). The red points on the track represent quasars at $z = 5.0, 5.5, 6.0,$ and 6.5 . The blue crosses denote all existing quasars known at $4.8 \leq z \leq 6.8$ (e.g., Fan et al. 2006; Willott et al. 2010; Mortlock et al. 2011; Venemans et al. 2015; Wu et al. 2015; Bañados et al. 2016, 2018; Jiang et al. 2016; Mazzucchelli et al. 2017; McGreer et al. 2018; Matsuoka et al. 2019a, 2019b; Pâris et al. 2017; Reed et al. 2019; Wang et al. 2016, 2018, 2019, 2021; Yang et al. 2017, 2019a, 2019b, 2020a, 2021), while the gray points and the black squares show the loci of M and L/T dwarfs (Kirkpatrick et al. 2011; Mace 2014; Best et al. 2015), respectively. The orange dashed lines bound the selected regions for $z \sim 5$ and $z \sim 6$ quasar candidates. Bottom: the $zW1W2$ color-color diagram. All symbols are the same as in the top panel. The orange dashed lines represent the cuts used for $z \sim 5$ and $z \sim 6$ quasar candidates. A more stringent $z - W1$ cut (orange dotted line) is used for the selection of $z > 6.4$ quasars. Note that the photometry in $W1$ and $W2$ are in the Vega system ($W1_{\text{Vega}} = W1_{\text{AB}} - 2.699$, $W2_{\text{Vega}} = W2_{\text{AB}} - 3.339$).

$z - W1/W1 - W2$ cuts (Figure 1, bottom). (4) Additionally, for objects that have $>3\sigma$ detections in the y_{P1} band, we use a $y_{P1} - W1$ color (Figure 2) to improve the purity. All objects without y_{P1} data are kept.

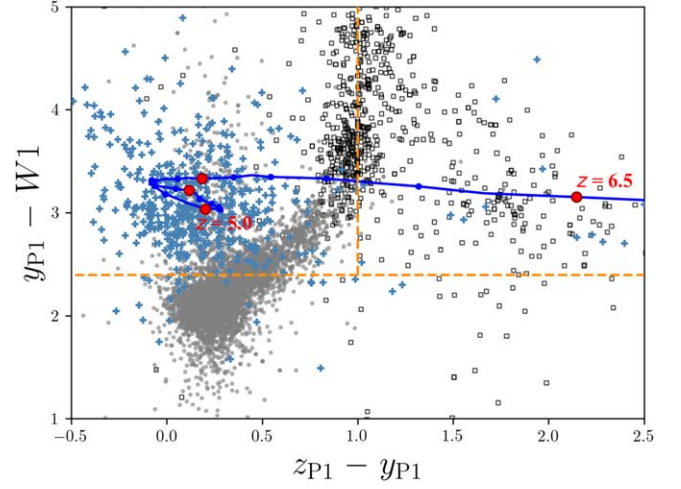


Figure 2. The $z_{P1}y_{P1}W1$ color-color diagram, used for the selection of $z \sim 6$ and 6.5 quasars. All symbols are the same as Figure 1. A $y_{P1} - W1$ cut is applied for all objects, and the two regions separated by the $z_{P1} - y_{P1}$ color (vertical orange dashed line) are the selections for $z \sim 6$ and $z > 6.4$ quasar candidates, respectively.

$z \sim 5.7\text{--}6.4$ quasar candidates. At $z \gtrsim 6$, the $\text{Ly}\alpha$ emission line moves into the z band. (1) Thus we first require the objects to be dropouts in the g and r bands (see criteria in Appendix A). (2) Then we select objects without i -band detection ($S/N_{iP1} < 3$) or meeting the cut of $i_{P1} - z > 2.0$. (3) We also apply the $z - W1/W1 - W2$ cuts, which are the same to the $z \sim 5$ selection. (4) In addition, if one object has $>3\sigma$ detections in the PS1 z and y bands, z_{P1} and y_{P1} photometry are employed to further reduce the contamination rate. The z_{P1} band covers a wavelength range bluer than the Legacy Surveys' z band, so it can provide additional constraints on colors. We limit $y_{P1} - W1 > 2.399$ and $z_{P1} - y_{P1} < 1.0$, as shown in Figure 2. Objects without z_{P1} and y_{P1} detections are kept.

$z > 6.4$ quasar candidates. (1) We first select objects that are dropouts in the gri bands (see criteria in Appendix A). (2) At the same time, we apply a more stringent $z - W1$ cut as shown in Figure 1 (bottom). (3) At such high redshift, most quasars only have the z -band detection, except for very luminous ones, which could be detected in the i band because of a bright $\text{Ly}\beta$ line. Thus, we require additional photometric data in the y_{P1} band for all candidates. We select objects with $>3\sigma$ detection in the y_{P1} and require $y_{P1} - W1 > 2.399$ (Figure 2). (4) We reject objects that have $>3\sigma$ detections in z_{P1} band but have colors of $z_{P1} - y_{P1} \leq 1.0$ (Figure 2) or $z_{P1} - W1 < 4.0$.

NIR photometry can play an important role in further rejecting M/L/T dwarf contaminants in high-redshift quasar selections by leveraging the power-law continuum of quasars. Among the NIR broad bands (i.e., $YJHK$), the J band has been mapped in the widest sky coverage. We therefore include J -band data into our selection, using photometry from UHS, ULAS, and VHS. We reject all objects that are covered by J -band photometry but have bad J -based colors (e.g., $J - W1 < 1.5$ or $y_{P1} - J > 2.0$ if y_{P1} is available; $J_{\text{AB}} = J_{\text{Vega}} + 0.938$). Objects without J -band data are kept.

In this first year of DESI observations, our high-redshift quasar selection focuses on a relatively bright candidate sample, with a z -band magnitude limit of 21.4 for $z \sim 5$ quasar candidates and 21.5 for $z \sim 6$ as well as $z > 6.4$ candidates.

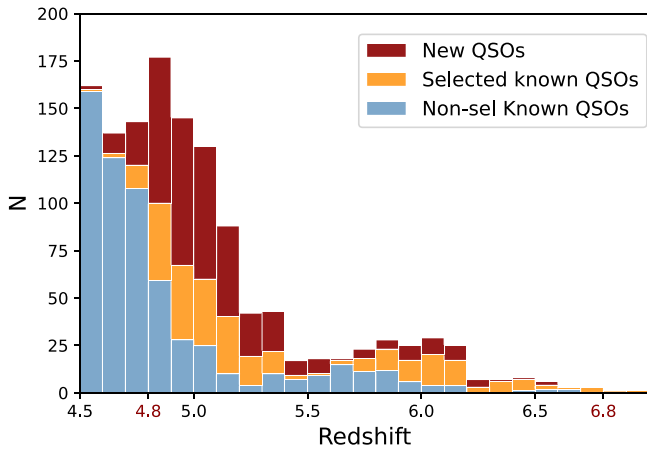


Figure 3. A stacked histogram presenting the redshift distribution of new quasars (red, “New QSOs”) from this survey, compared with all existing known quasars that are in the DESI footprint and within our survey depth (i.e., < 21.5 in the LS z band). Known quasars that pass our selections are shown in orange (“Selected known QSOs”), while the quasars that do not meet our selections are in the color of blue (“Non-sel Known QSOs”). The redshift range that our survey focuses on has been marked in red ($z = 4.8\text{--}6.8$).

This is already 1 mag deeper than the previous wide-area $z \sim 5$ quasar surveys (Wang et al. 2016; Yang et al. 2017, 2019a), while this depth only covers the luminous end of $z > 6$ quasar population. We will extend the quasar selections toward a fainter range in subsequent years of the DESI survey.

In total, we obtain ~ 3500 targets for $z \sim 5$ quasar selection, ~ 3000 targets for $z \sim 6$ selection, and ~ 450 targets for $z > 6.4$ quasars within the DESI footprint, with an average target density of 0.5 per square degree. These targets have a bit-name of Z5_QSO in the DESI target catalog. We are not excluding known quasars that pass our selection criteria in order to construct a uniformly observed spectral data set, which is important for future spectral analysis. Multiepoch spectra will also allow the study of quasar variability. At the survey depth, about 60–90% of known quasars can be selected by our selections in three different redshift ranges, as shown in Figure 3, which can be treated as a rough estimate of the selection completeness. A careful measurement of the selection function using a simulated quasar sample will be presented with our final quasar sample.

2.3. Selection of Quasars at $z \sim 4\text{--}5.3$ in SV1

In this paper, we also report results from a selection of $z \sim 4\text{--}5.3$ quasars using photometric data from the Legacy Surveys only, and this selection is used as a pilot selection during the DESI SV1 (DESI Collaboration et al. 2023a; Myers et al. 2023). DESI conducted SV observations, prior to the main, 5 yr mission, to validate the systems, to refine the purity and completeness of the targeting algorithms, and to stress-test the procedures that would be needed (DESI Collaboration et al. 2023a). SV1 is the first iteration of SV ran. The pilot survey of $z \sim 4\text{--}5.3$ quasars was designed to test the quasar selection without the i -band photometry. The selection was based on grz and $zW1W2$ colors. The selection first adopted the g -band and r -band dropout techniques. The $r - z$ color was applied instead of the riz colors, and the $zW1W2$ cuts were used with a relaxed $W1 - W2$ color ($W1 - W2 > 0.3$) for $z < 4.8$ quasars because

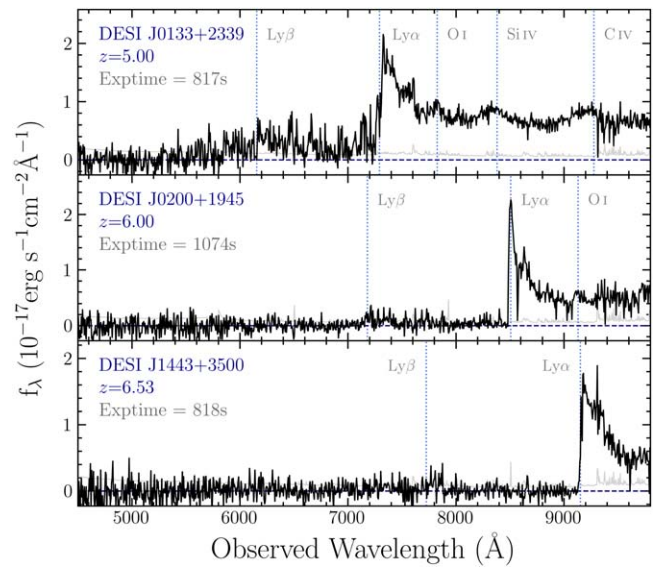


Figure 4. Examples of the DESI spectra for quasars at $z = 5, 6,$ and 6.5 , binned with 7 pixels. The three spectra are from observations with $\sim 800\text{--}1000$ s actual exposure time. These three quasars are 20.55, 20.72, and 21.20 mag in the Legacy Survey z band. The quasar broad emission lines (i.e., $\text{Ly}\beta$, $\text{Ly}\alpha$, O I, Si IV, and C IV) used for redshift measurements are marked with blue dotted lines. The spectra of all 412 new quasars are shown in Figure 7.

of the bluer $W1 - W2$ color of $z \sim 4.5$ quasars. The selection criteria are listed in Appendix B.

This selection yielded ~ 60 quasars during the SV1 observations between 2020 December and 2021 May. Among them, there were 38 new quasars at $3.8 \leq z \leq 5.7$, as listed in Table 2 and shown in Figure 8 in Appendix B. The selection of $z \sim 5$ quasars without i -band photometry could help construct a quasar sample that is independent of the $\text{Ly}\alpha$ line luminosity. Indeed, we were able to discover weak line (WL) quasars and broad absorption line (BAL) quasars at $z \sim 5$ (Figure 8), which are missed by the selection mentioned above and also by the quasar surveys in previous works (e.g., Wang et al. 2016; Yang et al. 2017, 2019a). However, the lack of i -band photometry led to a high contamination rate; the success rate of this selection was only 2–3%, which is quite low compared with the efficiency of our main selection described above (see details of efficiency in Section 3). Therefore, this selection was not retained after the SV observations. We publish the 38 new quasars discovered in SV1 in this paper.

3. Results from Observations in the First Year

3.1. Observations and Redshift Measurements

The selected $z \sim 4.8\text{--}6.8$ quasar candidates are mainly observed as dark-time targets in the DESI main survey, which started on 2021 May 14. A minor part (1.6%) of candidates were observed during the DESI 1% survey (SV3; in 2021 April) and the DESI SV1 (before 2021 April 4; for 27 targets overlapped with the SV1 selection). These targets have the same fiber assignment priority to the primary QSO targets (Schlafly et al. 2023). All our targets are designed to first have a single-exposure with an effective exposure time³⁷

³⁷ The effective exposure time is defined based on the spectroscopic average signal-to-noise ratio and is utilized to achieve required S/N in a minimum amount of time. More details can be found in Guy et al. (2023) and Schlafly et al. (2023). The exposure times reported later in this paper are all the actual exposure times.

(Guy et al. 2023) of 1000 s for the purpose of identification. An $S/N > 3$ per pixel is expected on the $Ly\alpha$ line to identify a target. Then all targets identified as quasars will be observed with three repeat exposures by DESI for high-quality spectra. As of 2022 May 14, ~ 2370 targets have been observed from our program, which is about 35% of the entire candidate sample. The spectra of our targets after a first-pass observation have sufficient S/N for quasar identification, as shown in Figure 4 and Figure 7.

We identify quasars using the daily coadd spectra in the database, which are products of the DESI spectroscopic pipeline (Guy et al. 2023). The spectroscopic pipeline is designed to extract spectra from the raw data, subtract sky model, flux-calibrate spectra based on standard star exposures, and then measure their classifications as well as redshifts. We identify quasars via visual inspection and estimate quasar redshifts from visual spectral fitting, which is not included in the general DESI spectra visual inspection (Alexander et al. 2023; Lan et al. 2023). The visual spectral fitting is based on a semiautomated toolkit, A Spectrum Eye Recognition Assistant (Yuan et al. 2013), which has been used to measure redshifts for a number of high-redshift quasars (e.g., Wang et al. 2016; Yang et al. 2017, 2019a; Wang et al. 2019). All spectra of our program have been visually inspected by at least two inspectors. When fitting spectra, we match the observed spectrum with the Sloan Digital Sky Survey (SDSS) quasar template based on quasars' broad emission lines, $Ly\beta$, $Ly\alpha$, O I, Si IV, and C IV if visible, as well as the continuum emission. Figure 4 shows three examples of the DESI spectra with emission lines identified. They represent the quality of single-epoch observation spectra used for our identification and visual spectral fitting. Such redshift measurements have a typical uncertainty of ± 0.03 (e.g., Wang et al. 2016; Yang et al. 2017). For weak line quasars and strong broad absorption line quasars, the uncertainty could be as large as ~ 0.05 – 0.1 . We have one primary inspector and at least one secondary inspector. If redshifts from primary and secondary inspectors have a difference ≤ 0.03 , we use redshift from the primary inspector. For a few cases in which we get a discrepancy > 0.03 , the inspectors repeat the VI together until they obtain a consistent result.

3.2. The Discovery of More Than 400 New Quasars

Among the observed targets, there are 556 quasars identified in the redshift range of $z \sim 4.4$ – 6.8 , including 144 known quasars and 412 new quasars. These new quasars span a redshift range from 4.44 to 6.53, with 220 quasars at $z \geq 5$ and 25 quasars at $z \geq 6$. The redshift distribution of these quasars is presented in Figure 3. So far, the observations of these targets result in an average success rate of 23% of quasars at $z > 4.7$. If we count the success rate of $z \sim 4.8$ – 5.4 , $z \sim 5.7$ – 6.4 , and $z > 6.4$ quasar selections separately, we obtain 39%, 8%, and 5%, respectively. The main contaminants are M/L/T dwarfs ($> 90\%$) and red galaxies, as shown in Appendix C (Figure 9). In Figure 4, we show examples of $z \sim 5$, 6, and 6.5 quasars newly identified from our program. Quasar DESI J144355+350055 at $z = 6.53$ is the highest-redshift new quasar identified from our survey to date.

Although our survey has not been completed, it has already significantly increased the number of quasars known at $z \geq 4.8$ (377 new quasars). The total number of known

quasars at $z = 4.8$ – 6.8 from previous works is about 810, and thus the new quasars from this program already expand the existing known quasar sample by 46%. At $z \geq 5$, our survey so far has increased the known quasar sample by more than one-third, with 220 new discoveries and 628 existing known quasars. Within the DESI footprint, our new discoveries have more than doubled the quasar sample size in the redshift range of 4.8–5.4.

We list all 412 new quasars in Table 1 and plot all spectra of these new quasars in Figure 7. The spectra plotted here are based on the coadd data of the DESI daily spectra. All spectral data will be made public in digital form in future DESI data releases (e.g., DESI Collaboration et al. 2023b).

3.3. Examples of Scientific Analysis

So far, the DESI high-redshift survey and the repeat observations of newly identified quasars have not been finished, so this sample is not complete enough for statistical analysis. However, there are already a number of spectra that have sufficient quality to allow us to start science analysis for individual objects.

As an example, Figure 5 shows the spectrum of quasar DESI J112903.54+023706.9, which has a z -band magnitude of 21.3, among the faintest targets in our candidate sample. The spectrum has ~ 4400 s exposure time, and the average S/N over the $Ly\alpha$ + N V line region is 9 per 0.8 \AA pixel and 3 per pixel on continuum. All quasars from this survey will be observed repeatedly by DESI to have comparable or longer exposure time. In addition, as shown in Figure 5, the Si IV and C IV BAL features can be seen clearly from this spectrum. The balmicity index BI (Weymann et al. 1991) is derived as ~ 2000 and 2500 km s^{-1} for the Si IV and C IV absorptions, respectively, using a 3 pixel binned spectrum. The BI (Weymann et al. 1991) is calculated by $BI = \int_{v_{\min}}^{v_{\max}} \left(1 - \frac{f(v)}{0.9}\right) C dv$, where $f(v)$ is the normalized spectrum, and C is set to 1 only when $f(v)$ is continuously smaller than 0.9 for more than 2000 km s^{-1} ; otherwise, it is set to 0.0. The value of v_{\min} is set to 0. The final spectral data set will allow us to identify BAL quasars and measure the BAL fractions at different redshift bins.

These quasar spectra also enable us to search for high-redshift DLA absorbers. Figure 6 shows an example of a $z = 4.018$ DLA identified in the spectrum of $z = 5.03$ quasar DESI J100828.30–021229.8. The spectrum has a coadd exposure time of ~ 5000 s. The redshift of this DLA is derived using a set of metal lines. Metal lines Si II $\lambda 1526$, C IV $\lambda 1548$, C IV $\lambda 1550$, Fe II $\lambda 1608$, and Al II $\lambda 1670$ have been identified. The column density of this DLA is determined as $\log N_{\text{HI}} = 21.2 \pm 0.2$ by fitting a Voigt profile. We place the centroid of a Voigt profile to the redshift of the low-ion metal-line transitions ($z = 4.018$) and manually select values of N_{HI} to fit the profile, assuming a single component of DLA plus possible blended $Ly\alpha$ forest in the wings. The uncertainties of N_{HI} estimations for high-redshift DLAs are dominated by continuum uncertainty and $Ly\alpha$ forest line blending (Rafelski et al. 2012). The column density of metal lines is derived from the apparent optical depth method using the routines publicly available in the LINETOOLS package (Prochaska et al. 2017). We then obtain $\log N = 14.64 \pm 0.03$ for Si using the Si II $\lambda 1526$ line, which implies a metallicity of -2.06 ± 0.21 . This follows the DLA metallicity-redshift evolution trend

Table 1
The 412 New Quasars from Our Main Selection

Name	R.A.	Decl.	z^a	z_{LS}
DESI J000147.64-035247.4	0.44850	-3.87986	5.27	20.79 ± 0.01
DESI J000232.92+131433.7	0.63716	13.24270	5.82	21.30 ± 0.04
DESI J000233.24+212725.0	0.63850	21.45695	6.19	21.47 ± 0.04
DESI J000503.75+214506.1	1.26562	21.75171	5.36	19.76 ± 0.01
DESI J000619.38+133649.6	1.58077	13.61380	4.86	21.19 ± 0.04
DESI J000918.00-101723.0	2.32500	-10.28972	5.33	21.27 ± 0.04
DESI J001040.04+115823.4	2.66682	11.97319	5.44	20.17 ± 0.01
DESI J001149.47+074520.5	2.95614	7.75570	4.92	19.61 ± 0.01
DESI J001744.71+230131.9	4.43631	23.02553	4.77	21.38 ± 0.04
DESI J001835.00+081559.4	4.64585	8.26652	5.34	21.05 ± 0.03
DESI J001912.13+043551.3	4.80056	4.59760	5.03	20.20 ± 0.01
DESI J002633.47+162937.5	6.63945	16.49376	5.10	21.35 ± 0.05
DESI J231627.96+213737.9	349.11649	21.62721	5.03	20.50 ± 0.02
DESI J231630.51-012428.4	349.12711	-1.40790	5.20	20.74 ± 0.01
DESI J232332.06+023848.4	350.88361	2.64679	5.11	20.94 ± 0.03
DESI J232911.44+021720.6	352.29767	2.28907	4.84	20.24 ± 0.01
DESI J233354.68-060522.9	353.47784	-6.08972	4.92	20.99 ± 0.03
DESI J233410.03-081702.3	353.54178	-8.28398	5.42	20.84 ± 0.03
DESI J233419.15-062626.2	353.57980	-6.44063	5.08	21.16 ± 0.04
DESI J233456.62-105351.5	353.73593	-10.89766	5.17	20.57 ± 0.02
DESI J233507.31+092725.3	353.78046	9.45705	5.20	21.26 ± 0.03
DESI J234216.88+050856.7	355.57034	5.14911	6.00	21.10 ± 0.02
DESI J235750.51-114244.5	359.46045	-11.71237	4.99	19.64 ± 0.01
DESI J235839.43+124708.8	359.66428	12.78578	4.64	20.89 ± 0.02

Notes.

^a Redshift from visual fitting using quasar template with a typical uncertainty of 0.03. For strong BAL quasars and WL quasars, the uncertainty could be ~ 0.05 – 0.1 . (This table is available in its entirety in machine-readable form.)

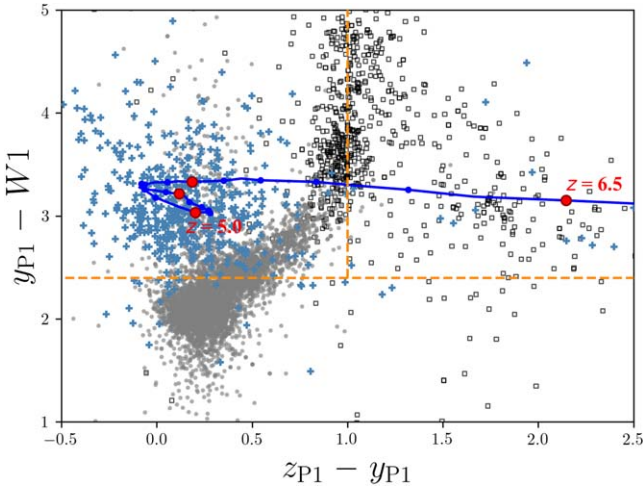


Figure 5. The DESI spectrum of a $z = 5.04$ quasar J112903.54+023706.9, coadded from four exposures with a total exposure time of ~ 4400 s. The spectrum plotted here is binned with 3 pixels for the BAL absorption measurements. The gray line is the spectral uncertainty. The target has a z -band magnitude of 21.3. This spectrum has sufficient S/N for quasar classification and study of strong absorption features. The Si IV and C IV BAL absorption troughs are denoted by the blue-shaded regions.

(Rafelski et al. 2012). A systematical search will be carried out using the complete DESI spectral sample.

In addition, we study radio detections among these new quasars by crossmatching ($2''$) new quasars with the catalogs from the Faint Images of the Radio Sky at Twenty centimeters (FIRST; Becker et al. 1995), the first epoch of the Very Large

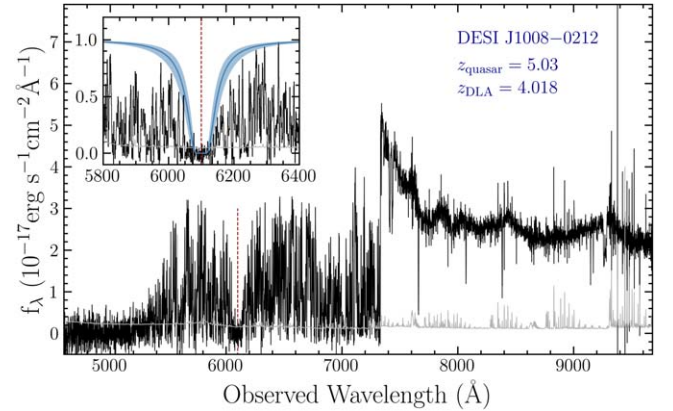


Figure 6. The DESI spectrum of a $z = 5.03$ quasar J100828.30-021229.8 without binning. The gray line represents the spectral uncertainty. A DLA system at $z = 4.018$ (red dashed line) is clearly present in the absorption spectrum. Its redshift is estimated using metal lines. The Voigt profile fitting (inset plot) yields a column density of $\log N_{\text{HI}} = 21.2 \pm 0.2$.

Array Sky Survey (VLASS; Gordon et al. 2020; Lacy et al. 2020), and the second data release from the ongoing LOW-Frequency ARray (LOFAR) Two-meter Sky Survey (LoTSS; Shimwell et al. 2022). The crossmatch radius is chosen following recent LOFAR studies (e.g., Retana-Montenegro & Röttgering 2018; Gloude-mans et al. 2022), although it might be small for matching the FIRST catalog. As a first test, we choose this radius for a reliable detection. We find six quasars detected in the FIRST catalog with peak flux densities from 1.2 to $54.7 \text{ mJy beam}^{-1}$ at 1.4 GHz. The same six objects are in the VLASS catalog. Two quasars have significant differences in

Table 2
The 38 New Quasars from the Selection in SV1

Name	R.A.	Decl.	z^a	z_{LS}
DESI J054840.05–223313.8	87.16687	–22.55383	4.63	20.38 ± 0.01
DESI J055103.87–233959.8	87.76612	–23.66664	3.91	20.72 ± 0.01
DESI J062712.07+481919.1	96.80030	48.32199	4.43	19.25 ± 0.01
DESI J065435.94+364333.9	103.64975	36.72609	4.61	19.66 ± 0.02
DESI J065918.89+364504.0	104.82872	36.75113	4.54	21.15 ± 0.03
DESI J071943.37+424955.2	109.93072	42.83202	5.09	21.21 ± 0.02
DESI J073853.30+182213.2	114.72207	18.37034	4.33	20.11 ± 0.01
DESI J081344.95+342726.8	123.43731	34.45746	5.23	20.68 ± 0.02
DESI J083558.88+321631.1	128.99533	32.27533	5.57	20.65 ± 0.02
DESI J090025.72+305706.6	135.10716	30.95184	4.41	20.68 ± 0.03
DESI J091332.51+314501.0	138.38547	31.75029	3.92	20.12 ± 0.01
DESI J091444.89+020337.8	138.68703	2.06051	4.41	19.87 ± 0.01
DESI J094314.99+642700.9	145.81244	64.45025	4.43	20.02 ± 0.01
DESI J095330.88+700140.8	148.37868	70.02802	5.32	21.05 ± 0.03
DESI J095519.52+021229.7	148.83131	2.20825	3.88	20.70 ± 0.02
DESI J095629.67+321432.7	149.12361	32.24243	5.15	21.14 ± 0.05
DESI J103049.13+320538.7	157.70470	32.09411	4.00	21.08 ± 0.03
DESI J103609.43+333654.0	159.03931	33.61501	4.32	21.29 ± 0.03
DESI J103630.59+311402.5	159.12747	31.23405	4.54	19.84 ± 0.01
DESI J104418.06+843435.9	161.07526	84.57666	4.30	19.94 ± 0.01
DESI J105805.63+332702.6	164.52344	33.45073	4.74	20.44 ± 0.01
DESI J111233.93+841901.5	168.14139	84.31708	5.07	20.48 ± 0.02
DESI J112612.76+830836.4	171.55316	83.14345	4.35	21.01 ± 0.03
DESI J112902.93+820927.5	172.26221	82.15764	4.33	18.82 ± 0.01
DESI J115329.59+283027.1	178.37328	28.50753	5.73	19.98 ± 0.02
DESI J115356.93+273711.5	178.48720	27.61987	3.97	20.52 ± 0.01
DESI J115537.05+282532.7	178.90436	28.42577	3.90	20.56 ± 0.02
DESI J115855.52+262912.6	179.73132	26.48685	4.23	20.50 ± 0.02
DESI J125214.84+262745.9	193.06181	26.46275	4.55	21.06 ± 0.04
DESI J130530.85+313944.1	196.37856	31.66225	3.91	20.84 ± 0.02
DESI J135716.95+225459.6	209.32062	22.91656	4.67	21.36 ± 0.03
DESI J135942.71+222634.2	209.92795	22.44285	4.85	21.20 ± 0.03
DESI J141550.25+311821.3	213.95940	31.30592	4.11	21.10 ± 0.03
DESI J141809.66–010502.3	214.54027	–1.08399	4.00	19.90 ± 0.01
DESI J150753.26+333228.9	226.97192	33.54136	4.36	20.69 ± 0.02
DESI J150931.23+175158.6	227.38013	17.86628	4.72	20.70 ± 0.03
DESI J163602.51+232043.0	249.01047	23.34530	4.54	21.25 ± 0.03
DESI J171717.79+444653.3	259.32413	44.78148	4.50	18.13 ± 0.002

Note.

^a Redshift from visual fitting using quasar template with a typical uncertainty of 0.03. For strong BAL quasars and WL quasars, the uncertainty could be ~ 0.05 – 0.1 . (This table is available in machine-readable form.)

the peak flux density between the measurements from FIRST and VLASS, which might be useful to study quasar radio variability. We also obtain 11 additional radio detections ($z \sim 4.7$ – 6.0) in the LoTSS DR2 catalog, with peak flux densities from 0.3 to 1.1 mJy beam^{–1} at 144 MHz. In the future, using the final sample, we will be able to measure the radio-loud fractions in different redshift bins.

4. Summary and Future Studies

In this paper, we describe a high-redshift ($z \sim 4.8$ – 6.8) quasar survey with DESI as a secondary program of the DESI survey. Using the photometric data from the Legacy Surveys DR9 (g , r , z , $W1$, and $W2$), the PS1 survey (i_{P1} , z_{P1} , and y_{P1}), and several NIR surveys (J), we carried out selections of quasars in three redshift ranges: $z \sim 4.8$ – 5.4 , 5.7 – 6.4 , and 6.4 – 6.8 . The observations during the DESI SV1 and the main

survey before 2022 May 14 have covered 35% of candidates and identified more than 550 quasars, yielding 412 new quasars at $4.44 \leq z \leq 6.53$, with 377 quasars at $z \geq 4.8$ and 220 at $z \geq 5.0$. The observations to date result in an average success rate of 23%. Assuming this success rate, we would expect ~ 1000 new quasars from this survey. The new discoveries from this survey have increased the sample size of known quasars by $\sim 46\%$ in the redshift range that we are targeting. The high-quality spectra allow us to start the study of individual quasar spectra, although the current data set is not yet complete enough for statistical analysis.

Based on this survey, we expect to construct a large $z \gtrsim 5$ quasar sample for scientific analyses. We will present details of the full quasar sample and the selection function when the identification of the entire sample is complete. The quasar luminosity functions will also be calculated at that time. In subsequent papers, we will present spectral fitting and basic

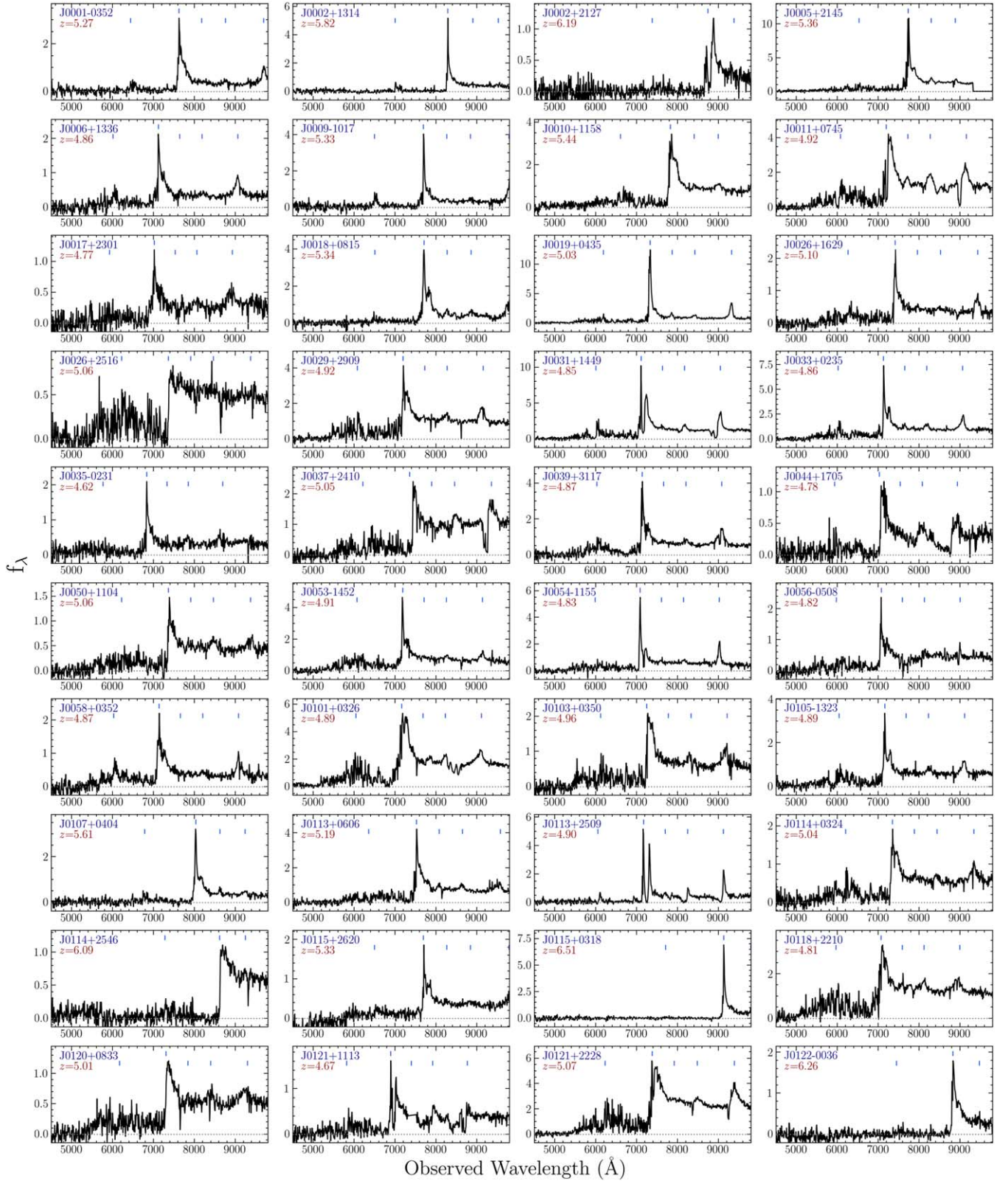


Figure 7. The single-exposure spectra of new quasars ordered as in Table 1, with an actual exposure time of ~ 500 –1800 s. The flux density (f_λ) is in units of $10^{-17} \text{ erg s}^{-1} \text{ cm}^{-2} \text{ \AA}^{-1}$. The spectra have been binned with 11 pixels for the purpose of plotting. The blue vertical lines denote the observed wavelengths of the emission lines, including (from left to right) Ly β , Ly α , O I, Si IV, and C IV. We present the first two pages of the spectral sample, and the complete figure set (412 spectra) is available online.

(The complete figure set (10 images) is available.)

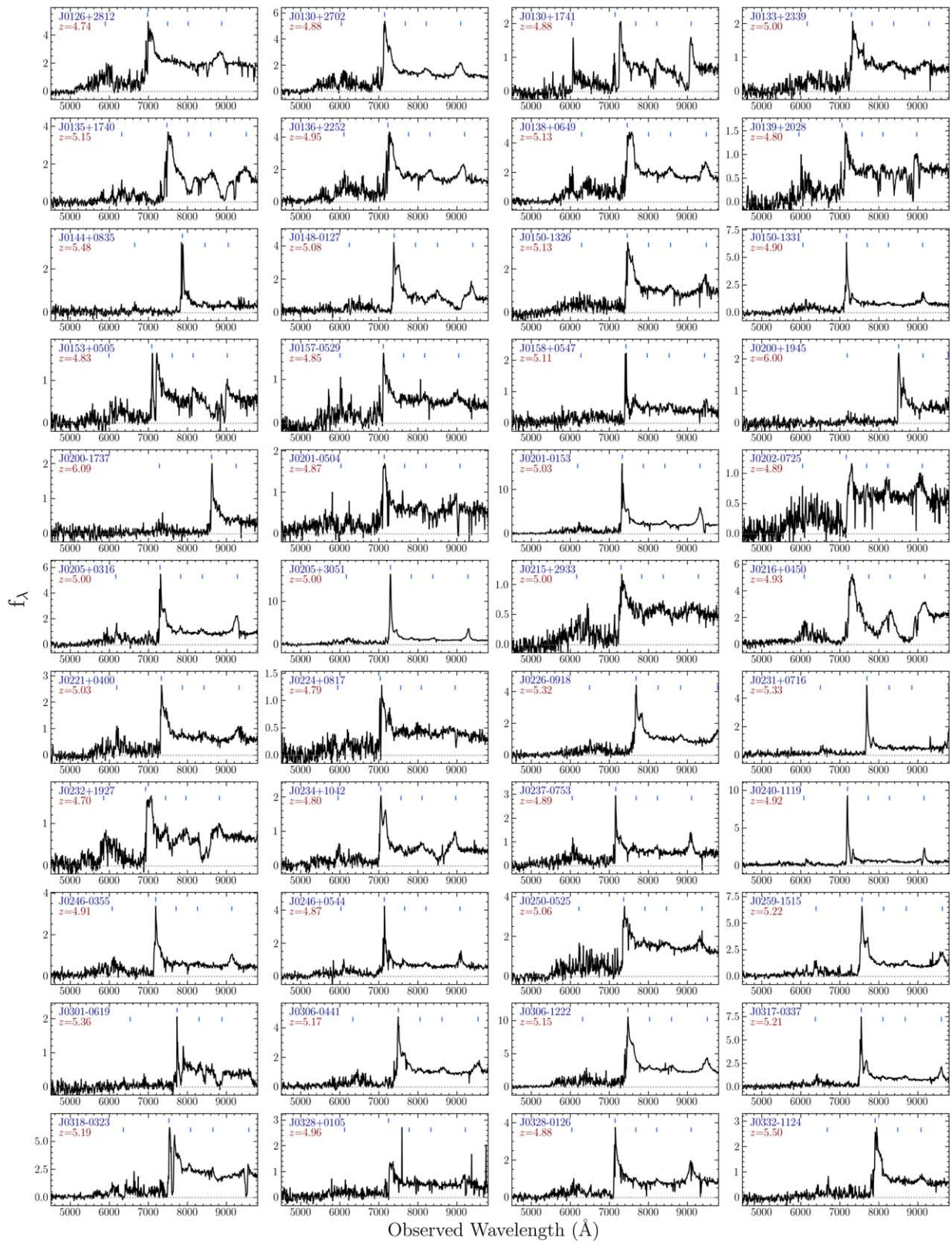


Figure 7. (Continued.)

quasar spectral properties (e.g., continuum slope, luminosity, and line width). When all repeat observations of quasars have been completed, the DESI quasar spectral data set will allow a set of science projects, including but not limited to $z \sim 5\text{--}6$ quasar

clustering, quasar proximity zone, IGM evolution, radio-loud fraction, WL and BAL quasar fractions, as well as intervening DLA and metal absorbers. Follow-up observations in the NIR will help build a sample for the study of early SMBH growth and the

BH mass function. We will also push the high-redshift quasar survey to a fainter magnitude in the future DESI survey.

Acknowledgments

We thank Alex Kim, Robert Knop, and Divij Sharma for the DESI internal database. X.F. acknowledges support from U.S. NSF grants AST 15-15115 and AST 19-08284, and NASA ADAP grant NNX17AF28G. A.D.M. was supported by the U.S. Department of Energy, Office of Science, Office of High-Energy Physics, under Award Number DE-SC0019022. F.W. acknowledges support by NASA through the NASA Hubble Fellowship grant No. HST-HF2-51448.001-A, and No. HF2-51434 awarded by the Space Telescope Science Institute, which is operated by the Association of Universities for Research in Astronomy Incorporated, under NASA contract NAS5-26555.

This material is based upon work supported by the U.S. Department of Energy (DOE), Office of Science, Office of High-Energy Physics, under Contract No. DE-AC02-05CH11231, and by the National Energy Research Scientific Computing Center, a DOE Office of Science User Facility under the same contract. Additional support for DESI was provided by the U.S. National Science Foundation (NSF), Division of Astronomical Sciences under Contract No. AST-0950945 to the NSF's National Optical-Infrared Astronomy Research Laboratory; the Science and Technology Facilities Council of the United Kingdom; the Gordon and Betty Moore Foundation; the Heising-Simons Foundation; the French Alternative Energies and Atomic Energy Commission (CEA); the National Council of Science and Technology of Mexico (CONACYT); the Ministry of Science and Innovation of Spain (MICINN), and by the DESI Member Institutions: <https://www.desi.lbl.gov/collaborating-institutions>.

The DESI Legacy Imaging Surveys consist of three individual and complementary projects: the Dark Energy Camera Legacy Survey (DECaLS), the Beijing-Arizona Sky Survey (BASS), and the Mayall z -band Legacy Survey (MzLS). DECaLS, BASS, and MzLS together include data obtained, respectively, at the Blanco telescope, Cerro Tololo Inter-American Observatory, NSF's NOIRLab; the Bok telescope, Steward Observatory, University of Arizona; and the Mayall telescope, Kitt Peak National Observatory, NOIRLab. NOIRLab is operated by the Association of Universities for Research in Astronomy (AURA) under a cooperative agreement with the National Science Foundation. Pipeline processing and analyses of the data were supported by NOIRLab and the Lawrence Berkeley National Laboratory. Legacy Surveys also uses data products from the Near-Earth Object Wide-field Infrared Survey Explorer (NEOWISE), a project of the Jet Propulsion Laboratory/California Institute of Technology, funded by the National Aeronautics and Space Administration. Legacy Surveys was supported by the Director, Office of Science, Office of High-Energy Physics of the U.S. Department of Energy; the National Energy Research Scientific Computing Center, a DOE Office of Science User Facility; the U.S. National Science Foundation, Division of Astronomical Sciences; the National Astronomical Observatories of China, the Chinese Academy of Sciences; and the Chinese National Natural Science Foundation. LBNL is managed by the Regents of the University of California under contract to the U.S.

Department of Energy. The complete acknowledgments can be found at <https://www.legacysurvey.org/>.

Any opinions, findings, and conclusions or recommendations expressed in this material are those of the author(s) and do not necessarily reflect the views of the U.S. National Science Foundation, the U.S. Department of Energy, or any of the listed funding agencies.

The authors are honored to be permitted to conduct scientific research on Iolkam Du'ag (Kitt Peak), a mountain with particular significance to the Tohono O'odham Nation.

Facilities: Mayall (DESI), Blanco (DECam), Mayall (Mosaic-3), Bok (90Prime), WISE, PS1 (GPC1), UKIRT (WFCam), VISTA (VIRCAM).

Appendix A

Selection Criteria for Survey of Quasars at $z \sim 4.8\text{--}6.8$

The survey of quasars at $z \sim 4.8\text{--}6.8$ has been described in Section 2.2. Here we present the full color-color selection criteria for each redshift range. The J , $W1$, and $W2$ magnitudes are used in the Vega systems ($J_{AB} = J_{\text{Vega}} + 0.938$, $W1_{AB} = W1_{\text{Vega}} + 2.699$, $W2_{AB} = W2_{\text{Vega}} + 3.339$). We performed a preselection to reduce the candidate sample size using the following criteria:

$$\begin{aligned} S/N(z) &> 5 \text{ and } z < 21.5; \\ S/N(W1) &> 3 \text{ and } S/N(W2) > 2; \\ S/N(g) &< 5 \text{ or } g > 24.5 \text{ or } g - r > 1.8; \\ S/N(r) &< 5 \text{ or } r - z > 1.0. \end{aligned} \quad (\text{A1})$$

We then matched the preselected sample with the PS1 photometric catalogs and applied color selections to select quasar candidates for different redshift ranges.

$z \sim 4.8\text{--}5.4$ quasar candidates:

$$\begin{aligned} S/N(g) &< 3 \text{ or } g - r > 2.5; \\ S/N(i_{P1}) &> 5 \text{ and } z < 21.4; \\ r - i_{P1} &> 0.8 \text{ and } r - i_{P1} < 3.0; \\ i_{P1} - z &< 0.5 \times (r - i_{P1}) - 0.2; \\ i_{P1} - z &> -0.5 \text{ and } i_{P1} - z < 0.7; \\ z - W1 &> 2.5 \text{ and } W1 - W2 > 0.5; \\ \text{If objects have PS1 } y_{P1} \text{ photometry,} \\ S/N(y_{P1}) &< 3 \text{ or } (y_{P1} - W1 > 2.399 \text{ and } z - y_{P1} < 0.5). \end{aligned} \quad (\text{A2})$$

$z \sim 5.7\text{--}6.4$ quasar candidates:

$$\begin{aligned} S/N(g) &< 3 \text{ or } g > 24.8; \\ S/N(r) &< 3 \text{ or } r > 24 \text{ or } r - z > 3; \\ S/N(i_{P1}) &< 3 \text{ or } i_{P1} - z > 2.0; \\ z - W1 &> 2.5 \text{ and } W1 - W2 > 0.5; \\ \text{If objects have PS1 photometry,} \\ S/N(z_{P1}) &< 3 \text{ or } S/N(y_{P1}) < 3 \text{ or} \\ ((S/N(i_{P1}) &< 3 \text{ or } i_{P1} - z_{P1} > 2.0) \text{ and } z_{P1} - y_{P1} < 1.0); \\ S/N(y_{P1}) &< 3 \text{ or } y_{P1} - W1 > 2.399. \end{aligned} \quad (\text{A3})$$

$z > 6.4$ quasar candidates:

$$\begin{aligned}
 & S/N(g) < 3 \text{ or } g > 25.0; \\
 & S/N(r) < 3 \text{ or } r > 25.0; \\
 & S/N(i_{p1}) < 3 \text{ or } i_{p1} > 23.5 \text{ or } i_{p1} - y_{p1} > 3.0; \\
 & z - W1 > 2.799 \text{ and } W1 - W2 > 0.5; \\
 & S/N(y_{p1}) > 3; \\
 & y_{p1} - W1 > 2.399 \text{ and } z - y_{p1} > 0.4; \\
 & \text{If objects have } z_{p1} \text{ photometry,} \\
 & S/N(z_{p1}) < 3 \text{ or } (z_{p1} - y_{p1} > 1.0 \text{ and } z_{p1} - W1 > 4.0).
 \end{aligned} \tag{A4}$$

Then, for objects with J -band detection ($S/N(J) > 3$), we applied J -band related colors to further reject contaminants by removing objects with the following colors:

$$y_{p1} - J > 2.0 \text{ or } J - W1 < 1.5. \tag{A5}$$

Appendix B

Selection of $z \sim 4\text{--}5.3$ Quasars in SV1

In Table 2, we list all 38 new quasars from the selection of $z \sim 4\text{--}5.3$ quasars during the DESI SV1 observations. The spectra are shown in Figure 8. We also list the selection criteria of this pilot SV selection below.

We first require g dropout and limit S/N in the z , $W1$, and $W2$ bands:

$$\begin{aligned}
 & S/N(g) < 3 \text{ or } g > 24.5 \text{ or } g - r > 1.8; \\
 & S/N(z) > 5; \\
 & S/N(W1) > 3, \quad S/N(W2) > 2.
 \end{aligned} \tag{B1}$$

Then, we build up different selection criteria for $z \sim 4\text{--}4.8$ and $z \sim 4.8\text{--}5.3$ quasars. $W1$ and $W2$ are in the Vega magnitude system.

$$\begin{aligned}
 & z \sim 4.8\text{--}5.3: \\
 & W1 - W2 > 0.5, \quad z - W1 > 2.0, \quad z - W1 < 4.5; \\
 & (S/N(r) < 3 \text{ or} \\
 & (r - z > 1.0 \text{ and } r - z < 3.9 \\
 & \text{and } r - z < (z - w1) \times 3.2 - 6.5) \\
 & \text{or } r - z > 4.4); \\
 & z < 21.4.
 \end{aligned} \tag{B2}$$

$$\begin{aligned}
 & z \sim 4\text{--}4.8: \\
 & W1 - W2 > 0.3, \quad z - W1 > 2.5, \quad z - W1 < 4.5; \\
 & (S/N(r) > 3, \quad r - z > -1.0, \quad r - z < 1.5; \\
 & z < 21.4.
 \end{aligned} \tag{B3}$$

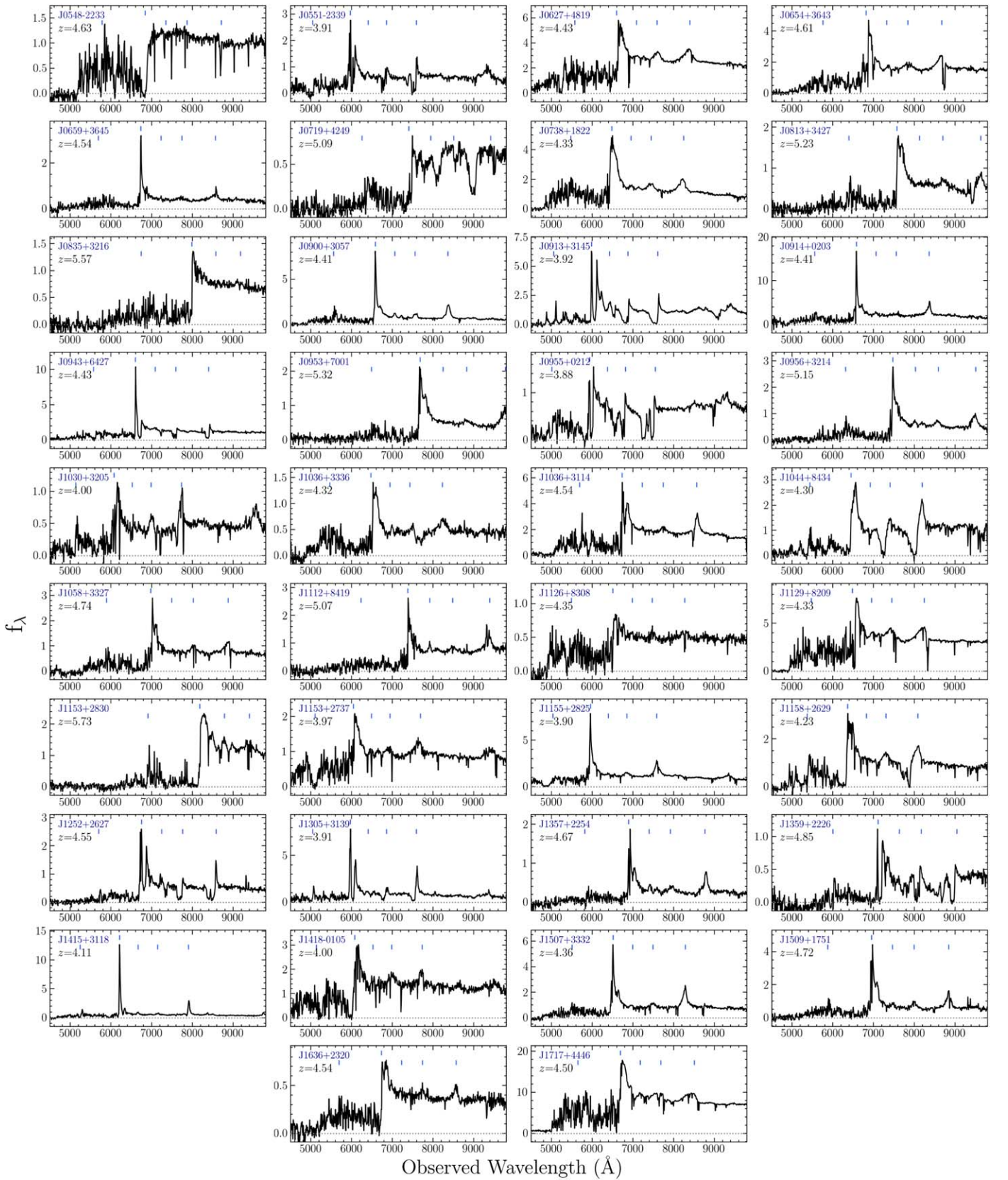


Figure 8. The spectra of new quasars from the SV1 selection ordered as in Table 2. The y-axis shows the flux density (f_λ) in units of $10^{-17} \text{ erg s}^{-1} \text{ cm}^{-2} \text{ \AA}^{-1}$. The spectra have been binned with 11 pixels for the purpose of plotting. The blue vertical lines denote the observed wavelengths of the emission lines, including (from left to right) Ly β , Ly α , O I, Si IV, and C IV. Quasar J0548-2233 is an example of WL quasar, and J0719+4249 is an example of BAL quasar.

Appendix C Contaminants

In Figure 9 we show example spectra of the main contaminants, M/L/T dwarfs and red galaxies, of our high-redshift quasar survey. We identify them using SDSS templates. One object cannot be certainly identified as a late-type M dwarf or an early-type L dwarf based on the current optical spectrum.

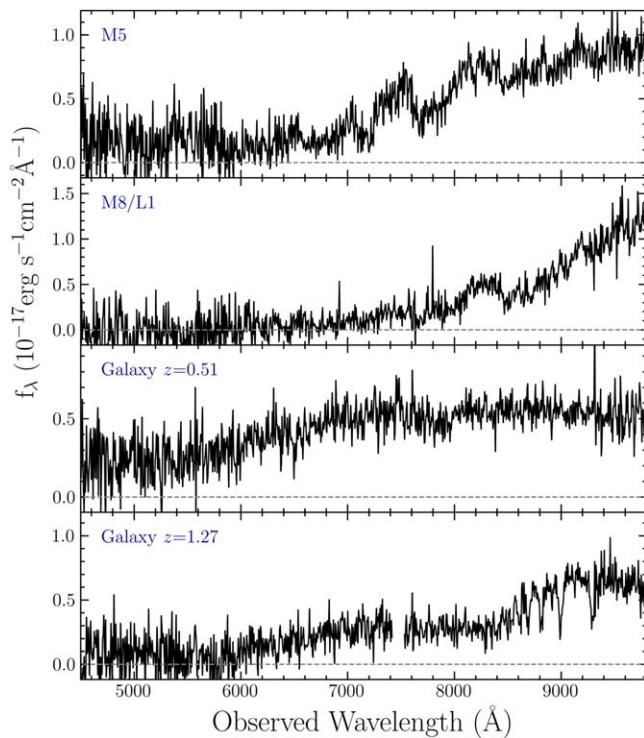


Figure 9. The example spectra of contaminants from our quasar survey, rebinned with 7 pixels. The first two are M dwarfs and the other two are galaxies. They all have red colors and thus contaminate the quasar selection.

ORCID iDs

Jinyi Yang <https://orcid.org/0000-0001-5287-4242>
 Xiaohui Fan <https://orcid.org/0000-0003-3310-0131>
 Ansh Gupta <https://orcid.org/0000-0003-4242-8606>
 Nathalie Palanque-Delabrouille <https://orcid.org/0000-0003-3188-784X>
 Feige Wang <https://orcid.org/0000-0002-7633-431X>
 Steven Ahlen <https://orcid.org/0000-0001-6098-7247>
 Kyle Dawson <https://orcid.org/0000-0002-0553-3805>
 Arjun Dey <https://orcid.org/0000-0002-4928-4003>
 Govinda Dhungana <https://orcid.org/0000-0002-5402-1216>
 Andreu Font-Ribera <https://orcid.org/0000-0002-3033-7312>
 Satya Gontcho <https://orcid.org/0000-0003-3142-233X>
 Stephanie Juneau <https://orcid.org/0000-0002-0000-2394>
 Theodore Kisner <https://orcid.org/0000-0003-3510-7134>
 Anthony Kremin <https://orcid.org/0000-0001-6356-7424>
 Laurent Le Guillou <https://orcid.org/0000-0001-7178-8868>
 Michael Levi <https://orcid.org/0000-0003-1887-1018>
 Paul Martini <https://orcid.org/0000-0002-4279-4182>
 Aaron Meisner <https://orcid.org/0000-0002-1125-7384>
 Ramon Miquel <https://orcid.org/0000-0002-6610-4836>
 John Moustakas <https://orcid.org/0000-0002-2733-4559>

Jundan Nie <https://orcid.org/0000-0001-6590-8122>
 Will Percival <https://orcid.org/0000-0002-0644-5727>
 Francisco Prada <https://orcid.org/0000-0001-7145-8674>
 Edward Schlafly <https://orcid.org/0000-0002-3569-7421>
 Gregory Tarlé <https://orcid.org/0000-0003-1704-0781>
 Risa Wechsler <https://orcid.org/0000-0003-2229-011X>
 Rongpu Zhou <https://orcid.org/0000-0001-5381-4372>
 Zhimin Zhou <https://orcid.org/0000-0002-4135-0977>
 Hu Zou <https://orcid.org/0000-0002-6684-3997>

References

- Abareshi, B., Aguilar, J., Ahlen, S., et al. 2022, *AJ*, 164, 207
 Alexander, D. M., Davis, T. M., Chaussidon, E., et al. 2023, *AJ*, 165, 124
 Allende Prieto, C., Cooper, A. P., Dey, A., et al. 2020, *RNAAS*, 4, 188
 Bañados, E., Venemans, B. P., Decarli, R., et al. 2016, *ApJS*, 227, 11
 Bañados, E., Venemans, B. P., Mazzucchelli, C., et al. 2018, *Natur*, 553, 473
 Becker, R. H., White, R. L., & Helfand, D. J. 1995, *ApJ*, 450, 559
 Best, W. M. J., Liu, M. C., Magnier, E. A., et al. 2015, *ApJ*, 814, 118
 Bosman, S. E. I., Davies, F. B., Becker, G. D., et al. 2022, *MNRAS*, 514, 55
 Chambers, K. C., Magnier, E. A., Metcalfe, N., et al. 2016, arXiv:1612.05560
 Chaussidon, E., Yèche, C., Palanque-Delabrouille, N., et al. 2023, *ApJ*, 944, 107
 Chen, S.-F. S., Simcoe, R. A., Torrey, P., et al. 2017, *ApJ*, 850, 188
 Cooper, A. P., Kposov, S. E., Allende Prieto, C., et al. 2023, *ApJ*, 947, 37
 Costa, T., Sijacki, D., Trenti, M., et al. 2014, *MNRAS*, 439, 2146
 DESI Collaboration, Adame, A. G., Aguilar, J., et al. 2023a, arXiv:2306.06307
 DESI Collaboration, Adame, A. G., Aguilar, J., et al. 2023b, arXiv:2306.06308
 DESI Collaboration, Aghamousa, A., Aguilar, J., et al. 2016a, arXiv:1611.00036
 DESI Collaboration, Aghamousa, A., Aguilar, J., et al. 2016b, arXiv:1611.00037
 Dey, A., Schlegel, D. J., Lang, D., et al. 2019, *AJ*, 157, 168
 D'Odorico, V., Feruglio, C., Ferrara, A., et al. 2018, *ApJL*, 863, L29
 Dye, S., Lawrence, A., Read, M. A., et al. 2018, *MNRAS*, 473, 5113
 Eilers, A.-C., Davies, F. B., & Hennawi, J. F. 2018, *ApJ*, 864, 53
 Fan, X., Carilli, C. L., & Keating, B. 2006, *ARA&A*, 44, 415
 Farina, E. P., Schindler, J.-T., Walter, F., et al. 2022, *ApJ*, 941, 106
 Gludemans, A. J., Duncan, K. J., Saxena, A., et al. 2022, *A&A*, 668, A27
 Gordon, Y. A., Boyce, M. M., O'Dea, C. P., et al. 2020, *RNAAS*, 4, 175
 Guy, J., Bailey, S., Kremin, A., et al. 2023, *AJ*, 165, 144
 Hahn, C., Wilson, M. J., Ruiz-Macias, O., et al. 2023, *ApJ*, 165, 253
 Jiang, L., McGreer, I. D., Fan, X., et al. 2016, *ApJ*, 833, 222
 Kelly, B. C., & Shen, Y. 2013, *ApJ*, 764, 45
 Kirkpatrick, J. D., Cushing, M. C., Gelino, C. R., et al. 2011, *ApJS*, 197, 19
 Lacy, M., Baum, S. A., Chandler, C. J., et al. 2020, *PASP*, 132, 035001
 Lan, T.-W., Tojeiro, R., Armengaud, E., et al. 2023, *ApJ*, 943, 68
 Lawrence, A., Warren, S. J., Almaini, O., et al. 2007, *MNRAS*, 379, 1599
 Levi, M., Bebek, C., Beers, T., et al. 2013, arXiv:1308.0847
 Lyke, B. W., Higley, A. N., McLane, J. N., et al. 2020, *ApJS*, 250, 8
 Mace, G. N. 2014, PhD thesis, Univ. of California, Los Angeles
 Mainzer, A., Bauer, J., Cutri, R. M., et al. 2014, *ApJ*, 792, 30
 Matsuoka, Y., Iwasawa, K., Onoue, M., et al. 2019a, *ApJ*, 883, 183
 Matsuoka, Y., Onoue, M., Kashikawa, N., et al. 2019b, *ApJL*, 872, L2
 Mazzucchelli, C., Bañados, E., Venemans, B. P., et al. 2017, *ApJ*, 849, 91
 McGreer, I. D., Fan, X., Jiang, L., et al. 2018, *AJ*, 155, 131
 McMahon, R. G., Banerji, M., Gonzalez, E., et al. 2013, *Msngr*, 154, 35
 Meisner, A. M., Lang, D., & Schlegel, D. J. 2017, *AJ*, 154, 161
 Meisner, A. M., Lang, D., & Schlegel, D. J. 2018, *RNAAS*, 2, 1
 Mortlock, D. J., Warren, S. J., Venemans, B. P., et al. 2011, *Natur*, 474, 616
 Myers, A. D., Moustakas, J., Bailey, S., et al. 2023, *AJ*, 165, 50
 Pâris, I., Petitjean, P., Ross, N. P., et al. 2017, *A&A*, 597, A79
 Prochaska, J. X., Tejos, N., Crighton, N., et al., 2017 linetools/linetools: Third Minor Release, v0.3, Zenodo, doi:10.5281/zenodo.1036773
 Rafelski, M., Wolfe, A. M., Prochaska, J. X., et al. 2012, *ApJ*, 755, 89
 Raichoor, A., Eisenstein, D. J., Karim, T., et al. 2020, *RNAAS*, 4, 180
 Raichoor, A., Moustakas, J., Newman, J. A., et al. 2023, *AJ*, 165, 126
 Reed, S. L., Banerji, M., Becker, G. D., et al. 2019, *MNRAS*, 487, 1874
 Retana-Montenegro, E., & Röttgering, H. 2018, *FrASS*, 5, 5
 Ross, N. P., & Cross, N. J. G. 2020, *MNRAS*, 494, 789
 Ruiz-Macias, O., Zarrouk, P., Cole, S., et al. 2020, *RNAAS*, 4, 187
 Schlafly, E. F., & Finkbeiner, D. P. 2011, *ApJ*, 737, 103
 Schlafly, E. F., Kirkby, D., Schlegel, D. J., et al. 2023, arXiv:2306.06309
 Schlegel, D. J., Finkbeiner, D. P., & Davis, M. 1998, *ApJ*, 500, 525
 Schneider, D. P., Richards, G. T., Hall, P. B., et al. 2010, *AJ*, 139, 2360

- Shen, Y., & Kelly, B. C. 2012, [ApJ](#), 746, 169
- Shen, Y., Wu, J., Jiang, L., et al. 2019, [ApJ](#), 873, 35
- Shimwell, T. W., Hardcastle, M. J., Tasse, C., et al. 2022, [A&A](#), 659, A1
- Silber, J. H., Fagrelus, P., Fanning, K., et al. 2023, [AJ](#), 165, 9
- The Dark Energy Survey Collaboration 2005, arXiv:[astro-ph/0510346](#)
- Venemans, B. P., Bañados, E., Decarli, R., et al. 2015, [ApJL](#), 801, L11
- Wang, F., Fan, X., Yang, J., et al. 2021, [ApJ](#), 908, 53
- Wang, F., Wu, X.-B., Fan, X., et al. 2016, [ApJ](#), 819, 24
- Wang, F., Yang, J., Fan, X., et al. 2018, [ApJL](#), 869, L9
- Wang, F., Yang, J., Fan, X., et al. 2019, [ApJ](#), 884, 30
- Weymann, R. J., Morris, S. L., Foltz, C. B., et al. 1991, [ApJ](#), 373, 23
- Willott, C. J., Delorme, P., Reylé, C., et al. 2010, [AJ](#), 139, 906
- Wright, E. L., Eisenhardt, P. R. M., Mainzer, A. K., et al. 2010, [AJ](#), 140, 1868
- Wu, X.-B., Wang, F., Fan, X., et al. 2015, [Natur](#), 518, 512
- Yang, J., Fan, X., Wu, X.-B., et al. 2017, [AJ](#), 153, 184
- Yang, J., Wang, F., Fan, X., et al. 2019a, [ApJ](#), 871, 199
- Yang, J., Wang, F., Fan, X., et al. 2019b, [AJ](#), 157, 236
- Yang, J., Wang, F., Fan, X., et al. 2020a, [ApJL](#), 897, L14
- Yang, J., Wang, F., Fan, X., et al. 2020b, [ApJ](#), 904, 26
- Yang, J., Wang, F., Fan, X., et al. 2021, [ApJ](#), 923, 262
- Yèche, C., Palanque-Delabrouille, N., Claveau, C.-A., et al. 2020, [RNAAS](#), 4, 179
- Yuan, H., Zhang, H., Zhang, Y., et al. 2013, [A&C](#), 3, 65
- Zhou, R., Dey, B., Newman, J. A., et al. 2023, [AJ](#), 165, 58
- Zhou, R., Newman, J. A., Dawson, K. S., et al. 2020, [RNAAS](#), 4, 181
- Zou, H., Zhou, X., Fan, X., et al. 2017, [PASP](#), 129, 064101